

Nettie R. Arnott\* and Yvette P. Richardson

The Pennsylvania State University, Department of Meteorology, University Park, Pennsylvania

Joshua M. Wurman

Center for Severe Weather Research, Boulder, Colorado

## 1. INTRODUCTION

Despite dedicated attention from the research community, predicting convection initiation (CI) remains a forecasting challenge, due in part to the coarseness of operational observing systems. Nevertheless, researchers have identified convergence lines such as the dryline and sea-breeze front as preferred locations of CI. For example, Atkins et al. (1995) observed horizontal convective rolls (HCRs) along a sea-breeze in Florida and found that their kinematic and thermodynamic properties played a significant role in CI. Similarly, Fankhauser et al. (1995) found that the merging of thunderstorm gust fronts with HCRs can lead to CI. Other favored locations include discontinuities or kinks along a front (Kingsmill, 1995). Often, small variations in surface moisture and temperature have a profound effect on whether thunderstorms form (Mueller et al. 1993).

Each of these studies suggests that observations of small-scale variations in the thermodynamic and kinematic fields are necessary for understanding the processes that initiate convection. To this end, the International H<sub>2</sub>O Project (IHOP) (Weckwerth et al. 2004) gathered many ground-based and airborne research platforms in order to observe the effects of small-scale inhomogeneities in initiating convection.

In accord with the goals of IHOP, this particular study uses mobile Doppler radar data with aircraft and sounding observations to document the structure and evolution of a cold front on 10 June 2002. These observations are used to explain the evolution of the cloud field and to understand why convection did not initiate in the radar-observed region of the cold front.

## 2. BACKGROUND

On 10 June 2002, four mobile radars formed an Intensive Observation Region (IOR) north of Ness City, KS (Fig. 1). Data were collected from 1928 UTC to 2118 UTC.

A slowly sagging cold front was draped across the Great Plains into Southern Colorado on the afternoon of 10 June 2002 (Fig. 2). Although the temperature and moisture gradients across the front were small (not uncommon for June in the Great Plains), its location is clearly delineated by the wind shift from southerly to north-northeasterly.

\*Corresponding author address: Nettie R. Arnott, The Pennsylvania State University, Dept. of Meteorology, University Park, PA 16802; email: narott@met.psu.edu

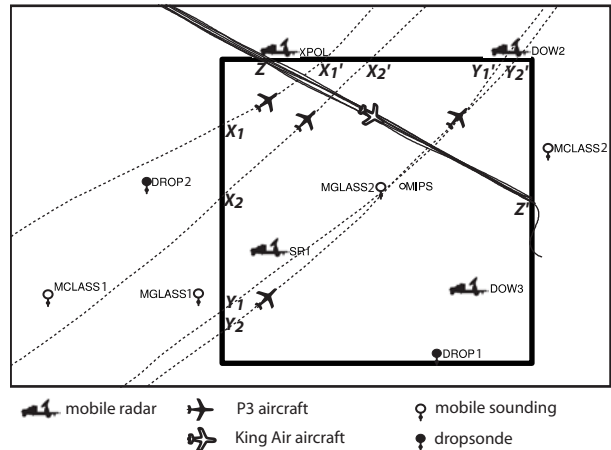


Fig. 1. IOR for 10 June 2002.

The 1200 UTC Dodge City, KS sounding (not shown) indicates moderate levels ( $1600 \text{ J kg}^{-1}$ ) of convective available potential energy (CAPE) with a deep mixed layer, dry air aloft, and the potential for very low convective inhibition (CIN) later in the day given sufficient surface heating. Thus, given the moderately favorable environment for CI, the decision was made to target the cold front near Ness City, Kansas (box in Fig. 2). Although cumuli developed in the IOR along the cold front during the deployment, deeper convection initiated along the cold front just southwest of the IOR.

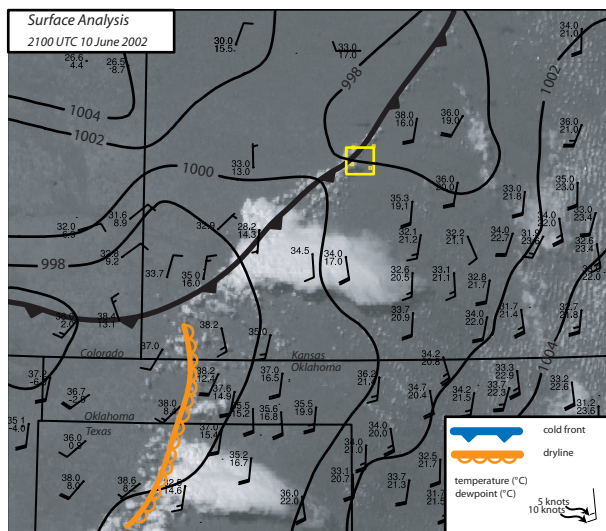


Fig. 2. Surface analysis with mean sea-level pressure contours. The small box in west-central KS is the IOR and depicts the bounds on subsequent analyses.

An MGLASS1 sounding taken within 5 km of the initiation location about 90 min. prior to initiation (not shown) reveals only small differences from the sounding taken within the grid domain an hour later (Fig. 3). With minimal CIN, both soundings indicate environments favorable for CI.

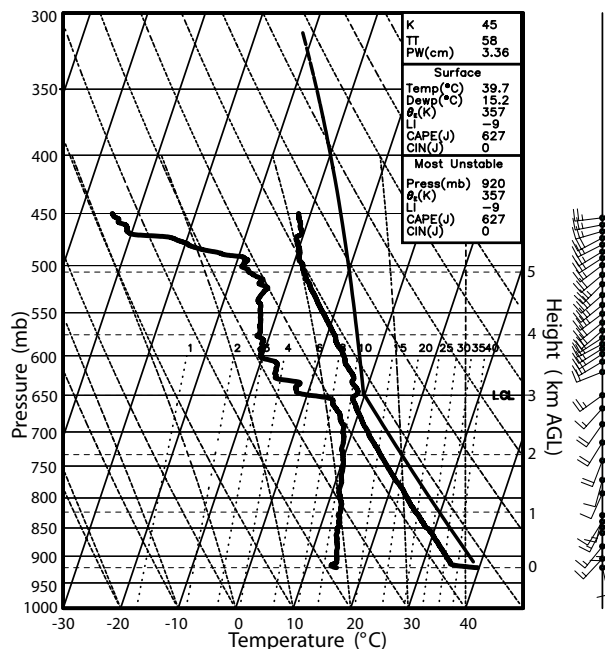


Fig. 3. Sounding on a SKEW-T from MGLASS2 at 2044 UTC, 10 June 2002. (See Fig. 1).

### 3. RADAR ANALYSIS METHODS

Two Doppler on Wheels (DOW) radars, the XPOL radar (3 cm wavelength,  $0.93^\circ$  beamwidth) (Wurman et al. 1997; Wurman 2001) and the Shared Mobile Atmospheric Research and Teaching Radar (SMART-Radar) (5 cm wavelength,  $1.5^\circ$  beamwidth) (Biggerstaff and Guynes 2000) collected data from 1928 to 2118 UTC. The radars scanned elevations from  $0.5^\circ$  to  $14.3^\circ$  above the horizontal with  $0.5^\circ$  increments below  $3.5^\circ$  and  $1.0^\circ$  increments at upper elevations. The DOW and XPOL radars collected a volume every 90 s, and the SMART-Radar collected a volume every 180 s. In order to minimize second trip echoes, DOW2 and DOW3 frequently changed the pulse repetition frequency (PRF), leading to varying degrees of oversampling in the azimuthal direction. Average non-oversampled beamwidth in the center of the IOR is 200 m. This allows for 100 m grid spacing in the objective analyses. The temporal and spatial resolution of the data collected on 10 June 2002 are much finer than in many previous CI studies, where temporal resolution was approximately 5 min and grid spacing was limited to 300 m or more (e.g. Wilson et al. 1992; Atkins et al. 1995; Kingsmill 1995), allowing for better characterization of the evolution of small scale features along the

front.

Before the radar data could be synthesized on a common earth-relative grid, several corrections were applied. After removing ground clutter and de-aliasing radial velocities, the data azimuths are made earth-relative by adding an offset based on the truck orientation determined using a solar alignment technique (Arnott et al. 2003). An advection correction was then applied using a technique described by Matejka (2002) to account for movement of features during the time required to collect a volume of radar data.

Barnes objective analyses were created using REORDER (Oye and Case 1992) with a smoothing parameter of  $0.264 \text{ km}^2$  and a cut-off radius of 1.54 km, based on recommendations of Pauley and Wu (1990). Over-determined dual-Doppler syntheses were produced using the Custom Editing and Display of Reduced Information in Cartesian Space (CEDRIC) (UCAR/NCAR) program using upward integration of the mass continuity equation to calculate vertical velocity ( $w$ ).

## 4. RESULTS

### 4.1 Kinematic frontal structure and evolution

Multi-Doppler derived convergence at 100 m AGL for four different times is shown in Fig. 4. The cold front, a secondary convergence line, linear reflectivity maxima (LRMs), which may be HCRs or gravity waves, and open cell convection are evident at 1946 UTC (Fig. 4a). At this time, convergence is evident along the entire length of the cold front. Note, however, that convergence along the cold front and the secondary boundary is variable spatially with local convergence maxima embedded in the background field. Between the two boundaries is a region of divergence. As the two convergence zones approach each other at 2010 UTC (Fig. 4b), the LRMs behind the cold front remain well defined, but the open cell convection becomes less clear and the divergent region between the two zones becomes smaller and more intense.

By 2037 UTC (Fig. 4c), however, convergence along the cold front has become more fragmented and the fine line becomes more contorted. Ninety second increment reflectivity loops from DOW2 indicate that the secondary convergence line has moved north, out of the domain.

Finally, at 2107 UTC, when deep convection initiates to the southwest, the convergence field in the IOR shows more complex structure compared with earlier times (Fig. 4d). Reasons for this evolution are discussed below.

Vertical vorticity maxima (misocyclones) are present along the front during the entire deployment (Fig. 5). The misocyclones often cause kinks in the reflectivity thin line and in the convergence and  $w$  fields (e.g. misocyclone 4 in Fig. 5a and misocyclone 6 in Fig. 5c). Typically,  $w$  maxima are associated with, but offset from the misocyclones. As misocyclones propagate along the front,

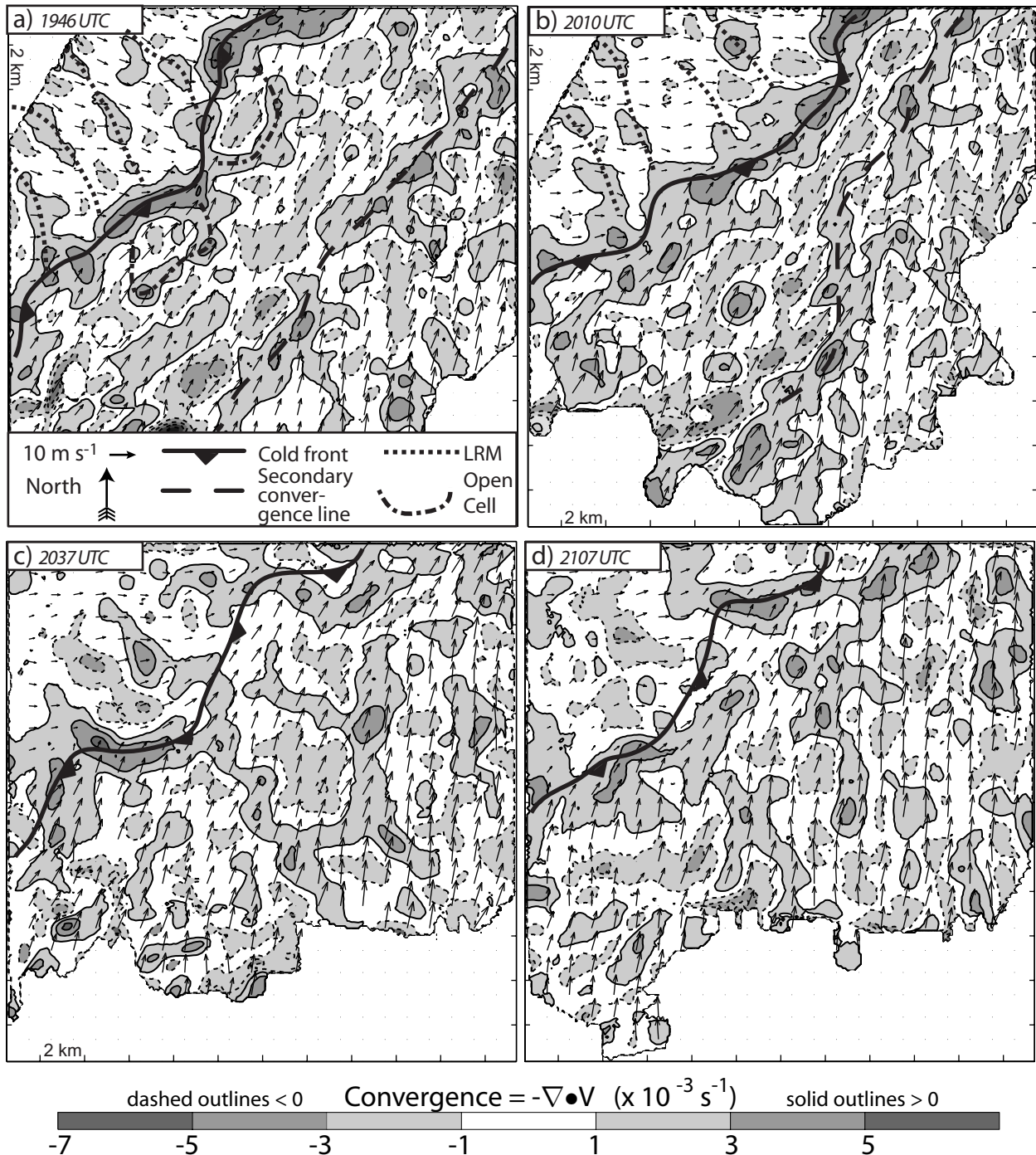


Fig. 4. Multi-Doppler syntheses at 100 m AGL. The center time of the volume is indicated in the top left corners. Horizontal wind vectors are plotted every 10 grid points (1 km).

between 1946 UTC (Fig. 5a) and 2010 UTC (Fig. 5b), they create small kinks and fractures in upward motion. After 2015 UTC, however, several misocyclone mergers occur, with the long axis of the merged misocyclones generally perpendicular to the front, causing exaggerated kinks or 'S'-shapes in  $w$  (misocyclones 6 and 7, Fig. 5c and d) (Marquis et al. 2004). This causes large fractures along the front in convergence and in  $w$ .

The fragmentation of convergence and  $w$  along the cold front has a significant impact on parcel trajectories. Parcels were chosen at 100 m AGL every 10 grid points (1 km) in a region straddling the cold front at 1953 UTC and at 2037 UTC (Fig. 7). The parcels were then traced backward and forward in time to map out their trajectories in the domain. Parcels entering the frontal circulation when convergence and  $w$  were more or less continuous

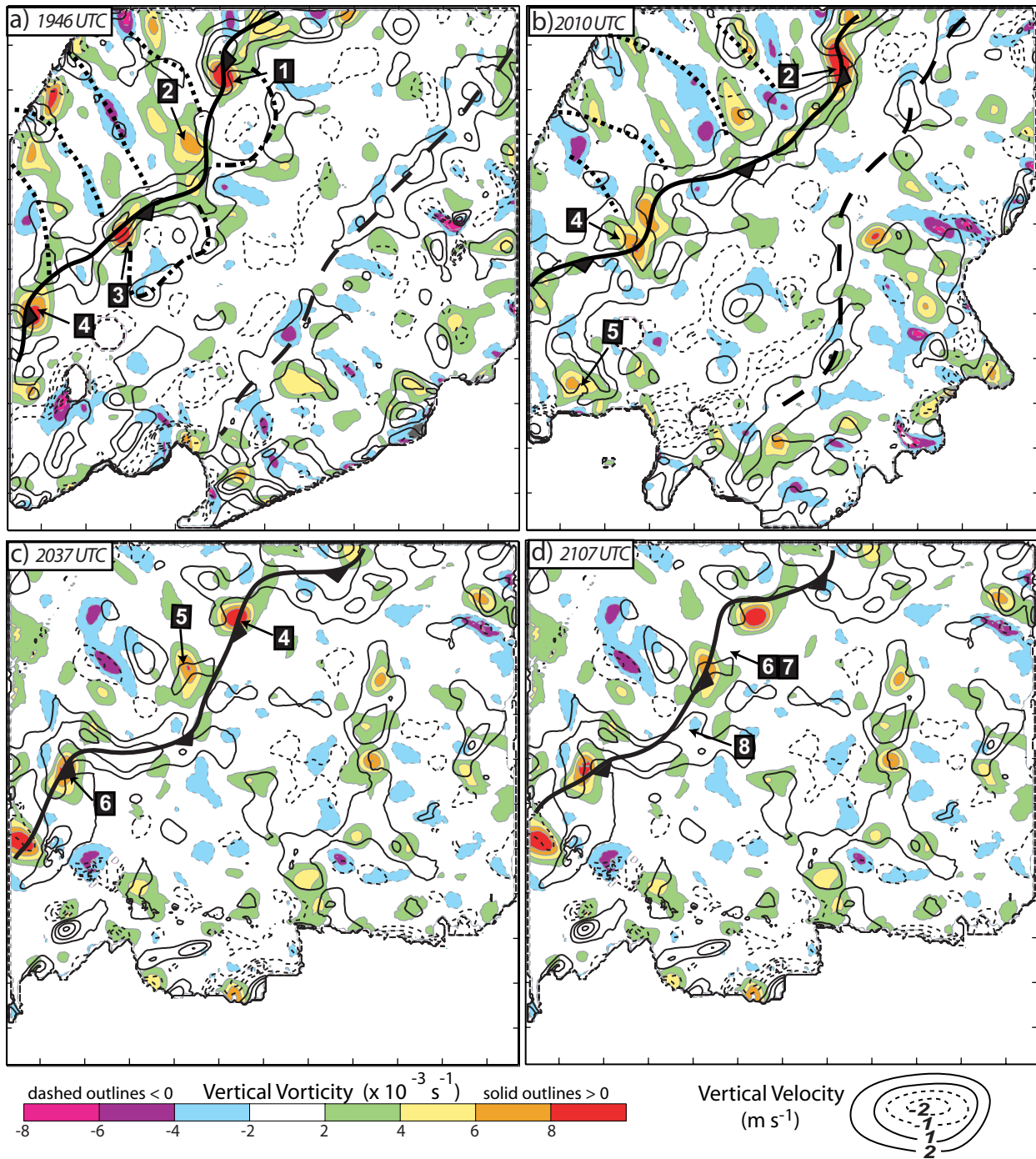


Fig. 5. Vertical velocity and vertical vorticity at 0.8 km AGL. The numbers indicate individual misocyclones referred to in the text.

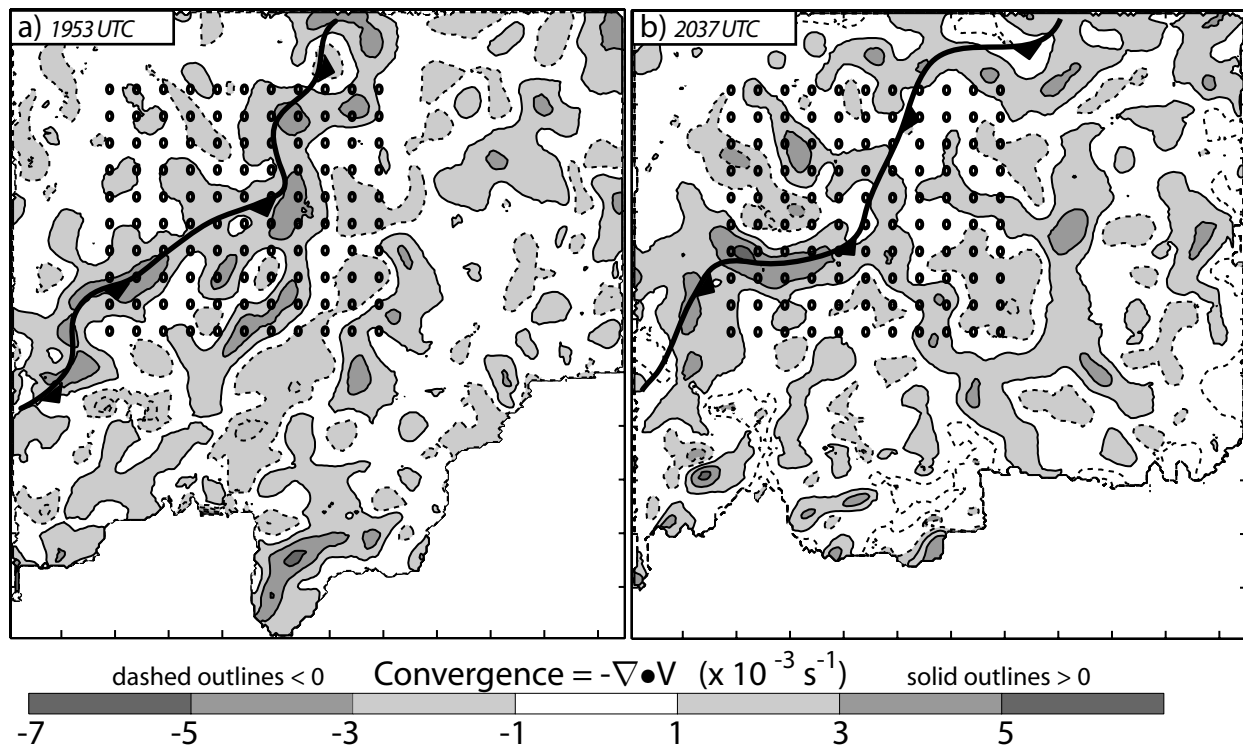


Fig. 6. Locations of parcels chosen for trajectories in Fig. 7. Note that as parcels are traced forward in time, the upward motion and convergence along the front begin to fracture (fracturing begins at 2020 UTC).

remained in regions of convergence as they moved along the front, and hence reached the top of the domain. In contrast, parcels entering the fracturing convergence zone experienced more complicated vertical excursions as they moved through the complex pattern of vertical velocity.

The convergence pattern is linked to the cloud field evolution using 1 km resolution visible satellite imagery (Fig. 8). Only scattered shallow cumulus were present in the IOR at 1955 UTC. The favorable trajectories at this time require approximately 9 min to travel from the top of the domain to cloud base. By 2000 UTC, the clouds were deeper, and scientists with DOW2 and DOW3 reported cumulus congestus clouds which also are evident in visible satellite imagery at 2020 UTC. Recall that around this time  $w$  began to fracture along the cold front. Nevertheless, the cumulus clouds are sustained for approximately 10 minutes more, consistent with the time it would take a parcel at the top of the domain to reach cloud base. IHOP scientists noticed a marked dissipation in cloud development at 2030 UTC which is evident in the visible satellite imagery at 2034 UTC. Cumulus clouds continue to diminish at 2039 UTC.

Therefore, we suggest that the unfavorable parcel trajectories resulting from the fractured  $w$  along the cold front cut off the supply of buoyant parcels to the clouds causing them to dissipate in the dry air above the boundary layer (Fig. 3). Hence, it appears that a continuous swath of convergence and  $w$  along the cold front was more favorable for deep cloud development all along the

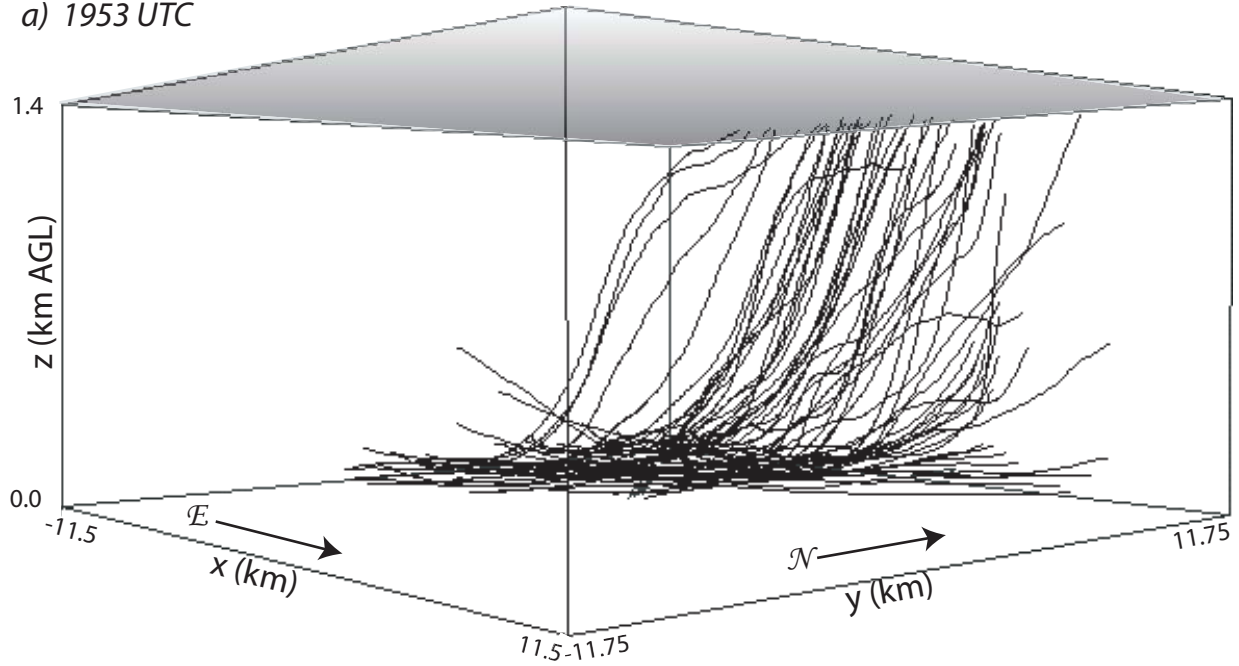
cold front than a fractured pattern, at least in this case where there was substantial along-front flow. Nevertheless, the magnitude of the maximum  $w$  did not lessen, but was associated with misocyclones near which the scattered clouds remained. Hence, misocyclones remained favorable locations for clouds as long as parcels remained in the  $w$  maxima associated with the misocyclones.

#### 4.2 Thermodynamic frontal structure and evolution

The P3 flew parallel to the cold front twice behind it and twice ahead of it (Fig. 1). Thermodynamic data were collected at 550 m AGL (on average) and are shown in Fig. 8. During its flight behind the front between 1938 UTC and 1940 UTC (Fig. 9a, thin line), the average potential temperature was 313.9 K, and ahead of the front between 1953 UTC and 1959 UTC the average potential temperature was 315.5 K (Fig. 9b, thin line), indicating a 1.6 K drop in potential temperature across the front.

The next flight behind the cold front (2017 UTC - 2020 UTC) indicates an average 1.5 K increase in potential temperature (Fig. 8a thick line) compared with the flight behind the boundary 40 minutes earlier. Ahead of the front, the average potential temperature increased only 0.4 K (Fig. 8b, thick line), indicating a weakening temperature gradient across the front. Potential temperature across the front recorded by the King Air at 170 m AGL shows only a 0.1 K difference in potential

a) 1953 UTC



b) 2037 UTC

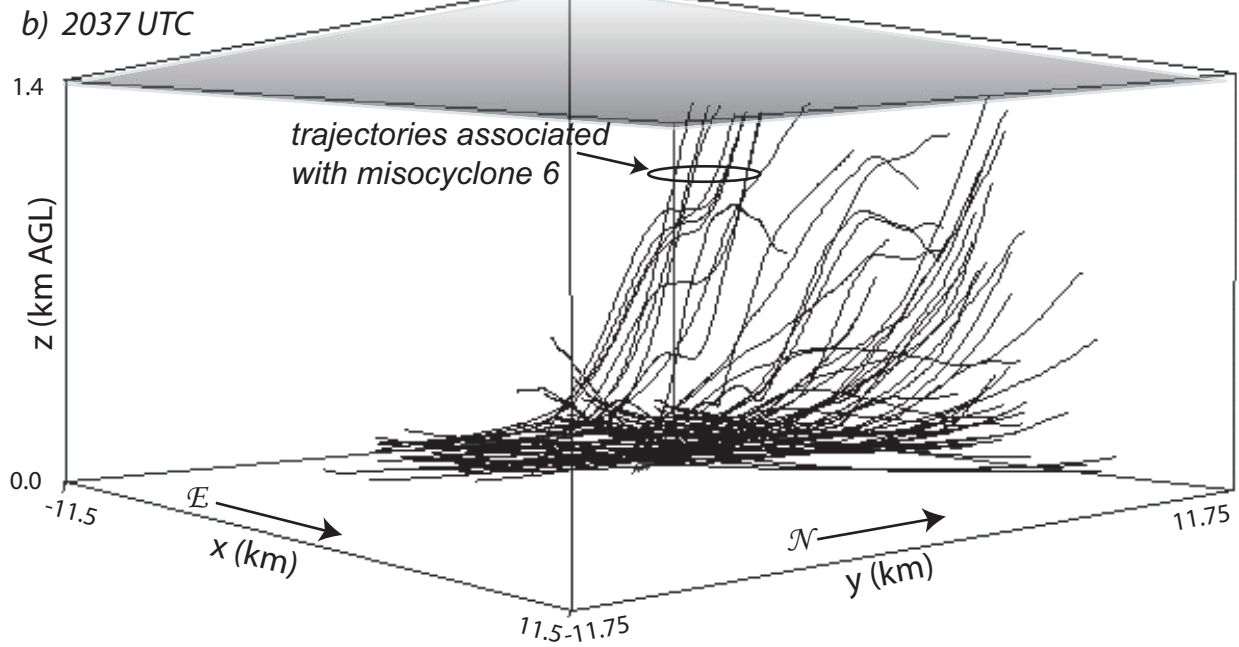


Fig. 7. Trajectories looking northwest towards cold front. Parcels not intersecting the top of the domain left the domain through one of the sides (usually the North side). All parcels were chosen at 100 m AGL and the trajectories trace the path the parcel took before and after the time indicated. (a) Parcels were chosen at 1953 UTC and traced back in time to 1928 UTC and forward in time to 2043 UTC when all parcels had left the domain. (b) Parcels were chosen at 2037 UTC and traced back in time to 2010 UTC and forward in time to 2118 UTC when all parcels had left the domain. The vertical lines correspond to the corners of the grid box.

temperature between the two P3 paths behind the front, indicating most of the warming is a temporal variation, not a spatial variation.

To determine the changes in the frontal circulation, a coordinate transformation is performed such that the new  $x$ -axis ( $x'$ ) is roughly parallel to the cold front and the new  $y$ -axis ( $y'$ ) is perpendicular to the cold front. Horizontal winds were also transformed such that  $u$  is along  $x'$  and  $v$  is along  $y'$ . Then,  $u$ ,  $v$ , and  $w$  were averaged along a piecewise function that approximates the cold front orientation. The averaging reduces the data to only the  $y'$  and  $z$  dimensions, yielding an average vertical cross section across the frontal zone (Fig. 10). Vertical velocity associated with the cold front is greater at 1946 UTC (Fig. 10a) than that at 2037 UTC (Fig. 10b). Hence, the cold frontal circulation has weakened, presumably due to the enhanced warming behind the cold front.

## 5. CONCLUSIONS

Four mobile radars observed a cold front between 1928 and 2118 UTC on 10 June 2002. During the first hour of the deployment, cumulus clouds developed and deepened along the cold front. During this time, convergence and  $w$  were nearly continuous along the front. By 2020 UTC, however, misocyclones created large contortions in the weakening cold front and in doing so, the misocyclones fractured convergence and  $w$  along the front.

When positive  $w$  was continuous along the cold front, parcels entering the frontal circulation remained in regions of upward motion as they were advected horizontally by the along-frontal flow, allowing many of them to reach the top of the domain, and presumably cloud base as suggested in photographs and visible satellite imagery. After the misocyclones caused significant fractures in positive  $w$  along the cold front, however, parcels entering the frontal circulation encountered both upward and downward motion as they were advected by the along-front winds. These parcels did not stay in regions of upward motion long enough to reach the top of the domain before encountering regions of downward motion, except for the few fortuitous parcels located in enhanced  $w$  near misocyclones. Thus, the clouds in the IOR evolved from a line along the front to scattered clouds associated with misocyclones.

Thus, we envision a complex interplay between the frontal circulation and the vertical velocity patterns associated with the smaller-scale features. On 10 June 2002 the frontal circulation weakened, allowing misocyclones to more readily distort the vertical velocity pattern such that alternating upward and downward motion were apparent along the front at later times, particularly during times of complex misocyclone interactions such as mergers. Parcels required significant dwell time in regions of positive  $w$  to reach the high cloud base, but their strong along-front motion caused them to enter regions of negative  $w$  and to descend. The weakening frontal circulation in time decreased the amount of

upward motion present along the front and decreased the area of positive  $w$  along the front. Cloud growth dissipated as fewer parcels remained in a region of upward motion as they attempted to ascend along the front. The existing clouds were then left to evaporate in the dry air above the boundary layer, preventing CI in the IOR.

## Acknowledgements

Thanks to Paul Markowski for providing several computer codes and for helpful discussions pertaining to this work. Comments from Ken Davis and Tammy Weckwerth are greatly appreciated. Robert Hart wrote the GrADS script to plot the Skew-T sounding. This work was supported by an American Meteorology Society Graduate Fellowship sponsored by ITT Industries, a National Science Foundation Graduate Research Fellowship, and National Science Foundation Grant ATM-0208651.

## REFERENCES

- Arnott, N. R., Y. P. Richardson, J. M. Wurman, and J. Lutz, 2003: A solar alignment technique for determining mobile radar pointing angles. Preprints, *31st Conference on Radar Meteorology*, 6-12 August, 2003, Seattle, WA., Amer. Meteor. Soc. 778-781.
- Atkins, N. T., R. M. Wakimoto, and T. M. Weckwerth 1995: Observations of the sea-breeze front during CaPE. Part II: Dual-Doppler and aircraft analysis. *Mon. Wea. Rev.*, **123**, 994-969.
- Biggerstaff, M. I., and J. Guynes, 2000: A new tool for atmospheric research. *20th Conf. on Severe Local Storms*, Orlando, Amer. Meteor. Soc., 277-280.
- Fankhauser, J.C., N.A. Crook, J. Tuttle, L.J. Miller, and C.G. Wade, 1995: Initiation of deep convection along boundary layer convergence lines in a semitropical environment. *Mon. Wea. Rev.*, **123**, 291-313.
- Kingsmill, D.E., 1995: Convection initiation associated with a sea-breeze front, a gust front, and their collision. *Mon. Wea. Rev.*, **123**, 2913-2932.
- Matejka, T., 2002: Estimating the most steady frame of reference from Doppler radar data. *J. Atmos. Oceanic Technol.*, **19**, 1035-1048.
- Marquis, J. N., Y. P. Richardson, and J. M. Wurman, 2004: Observations of misocyclones along boundaries during IHOP. Preprints: *22nd Conf. on Severe Local Storms*, 4-8 October, 2004, Hyannis, MA., Amer. Meteor. Soc., this issue.
- Mueller, C.K., J. W. Wilson, and N. A. Crook, 1993: The utility of sounding and mesonet data to nowcast thunderstorm initiation. *Wea. Forecasting*, **8**, 132-146.

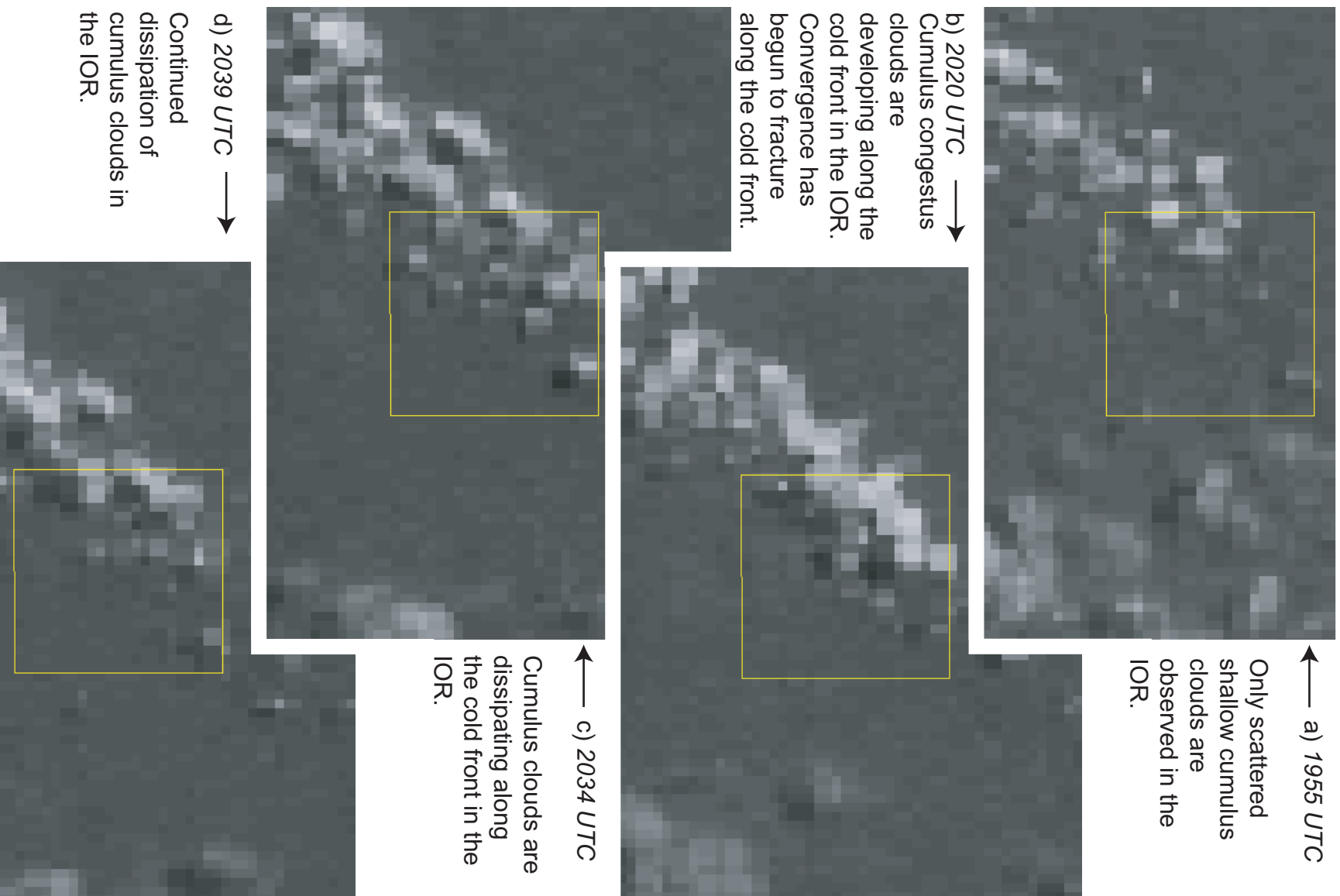


Fig. 8. Evolution of cumulus clouds in 1 km visible satellite imagery.

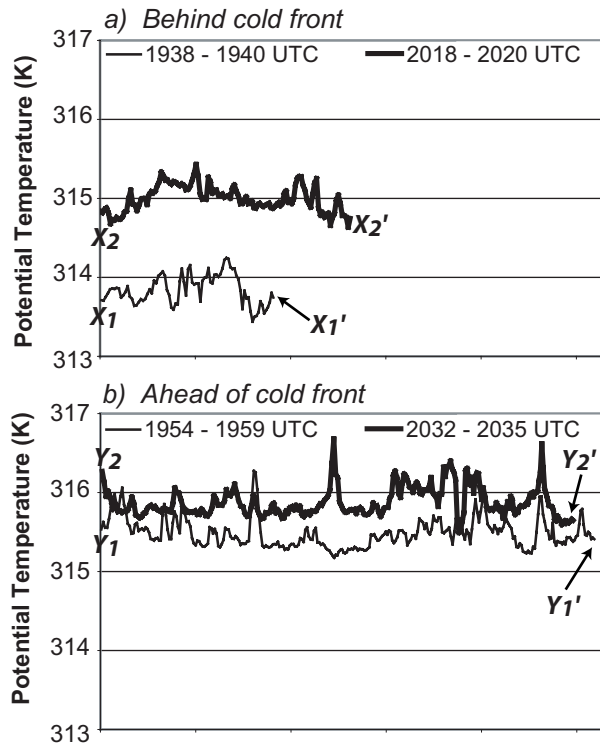


Fig. 9. P3 1Hz potential temperature (a) behind and (b) ahead of the cold front. X-X' and Y-Y' indicate the P3 track in Fig. 1 along which the data were collected.

- Oye, R., and M. Case, 1992: REORDER- A program for gridding radar data: Installation and use manual for the UNIX version. 22pp. [Available from Field Observing Facility, NCAR, P.O. Box 3000, Boulder, CO., 80307].
- Pauley, P.M. and X. Wu, 1990: The theoretical, discrete, and actual response of the Barnes objective scheme for one- and two- dimensional fields. *Mon. Wea. Rev.*, **118**, 1145-1163.
- \_\_\_\_\_, D. B. Parsons, S. E. Koch, J. A. Moore, M. A. LeMone, B. B. Demoz, C. Flamant, B. Geerts, J. Wang, and W. F. Feltz, 2004: An overview of the International H2O Project (IHOP\_2002) and some preliminary highlights. *Bull. Amer. Meteor. Soc.*, **85**, 253-277.
- Wilson, J. W., G. B. Foote, N. A. Crook, J. C. Fankhauser, C. G. Wade, J. D. Tuttle, and C. K. Mueller, 1992: The role of boundary-layer convergence zones and horizontal rolls in the initiation of thunderstorms: A case study. *Mon. Wea. Rev.*, **120**, 1785-1814.
- Wurman, J. M., J. Straka, E. Rasmussen, M. Randall, and A. Zahrai, 1997: Design and development of a portable, pencil-beam, pulsed, 3-cm Doppler radar. *J. Atmos. Oceanic. Technol.*, **14**, 1502-1512.

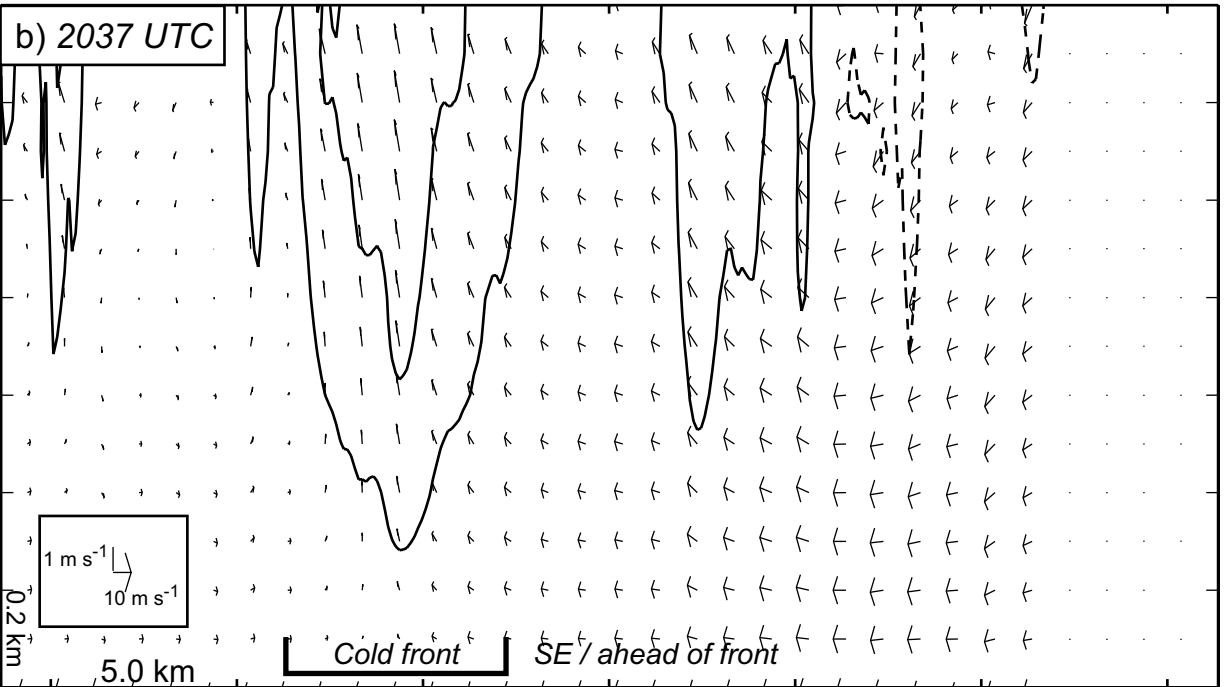
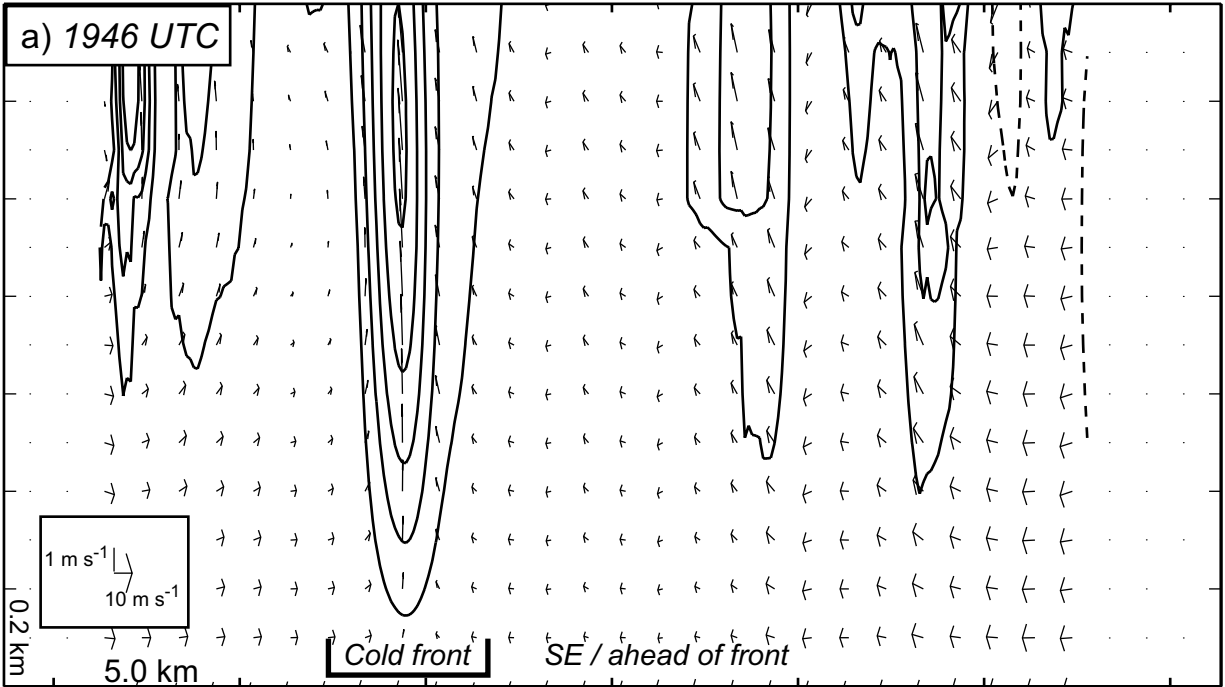


Fig. 10. Vertical velocity contoured every  $0.5 \text{ m s}^{-1}$  (positive values with bold contours, negative values with thin contours, 0 contour not shown) and winds in the plane of an average vertical cross section across the cold front. Vertical velocity greater than  $1 \text{ m s}^{-1}$  is shaded.